Journal of Nanobiotechnology

RESEARCH

Open Access

Living photosynthetic microneedle patches for in situ oxygenation and postsurgical melanoma therapy

Jinxuan Jia[1,2,3], Xuhong Guo[1], Yuwei Wang[1], Meiling Wu[4], Xiaocheng Wang[2*], Miaoqing Zhao[5*] and Yuanjin Zhao[1,6*]

Abstract

Surgical excision remains the principal treatment for melanoma, while tumor recurrence and delayed wound healing often occur due to the residual tumor cells and hypoxic microenvironment in the postoperative skin wounds. Herein, we present a living photosynthetic microneedle (MN) patch (namely MA/CM@MN) loaded with microalgae (MA) and cuttlefish melanin (CM) for postsurgical melanoma therapy and skin wound healing. Benefiting from the oxygenic photosynthesis of the alive MA in the MN base, the MA/CM@MN can generate oxygen under light exposure, thus facilitating skin cell proliferation and protecting cells against hypoxia-induced cell death. In addition, with CM nanoparticles embedded in the MN tips, the MA/CM@MN can be effectively heated up under near-infrared (NIR) irradiation, contributing to a strong tumor killing efficacy on melanoma cells in vitro. Further experiments demonstrate that the NIR-irradiated MA/CM@MN effectively prevents local tumor recurrence and simultaneously promotes the healing of tumor-induced wounds after incomplete tumor resection in melanoma-bearing mice, probably because the MA/CM@MN can inhibit tumor cell proliferation, stimulate tumor cell apoptosis, and mitigate tissue hypoxia in light. These results indicate that the living photosynthetic MN patch offers an effective therapeutic strategy for postoperative cancer therapy and wound healing applications.

*Correspondence:
Xiaocheng Wang
wangxiaocheng@ucas.ac.cn
Miaoqing Zhao
zhaomqsd@163.com
Yuanjin Zhao
yjzhao@seu.edu.cn

Full list of author information is available at the end of the article

Graphical Abstract

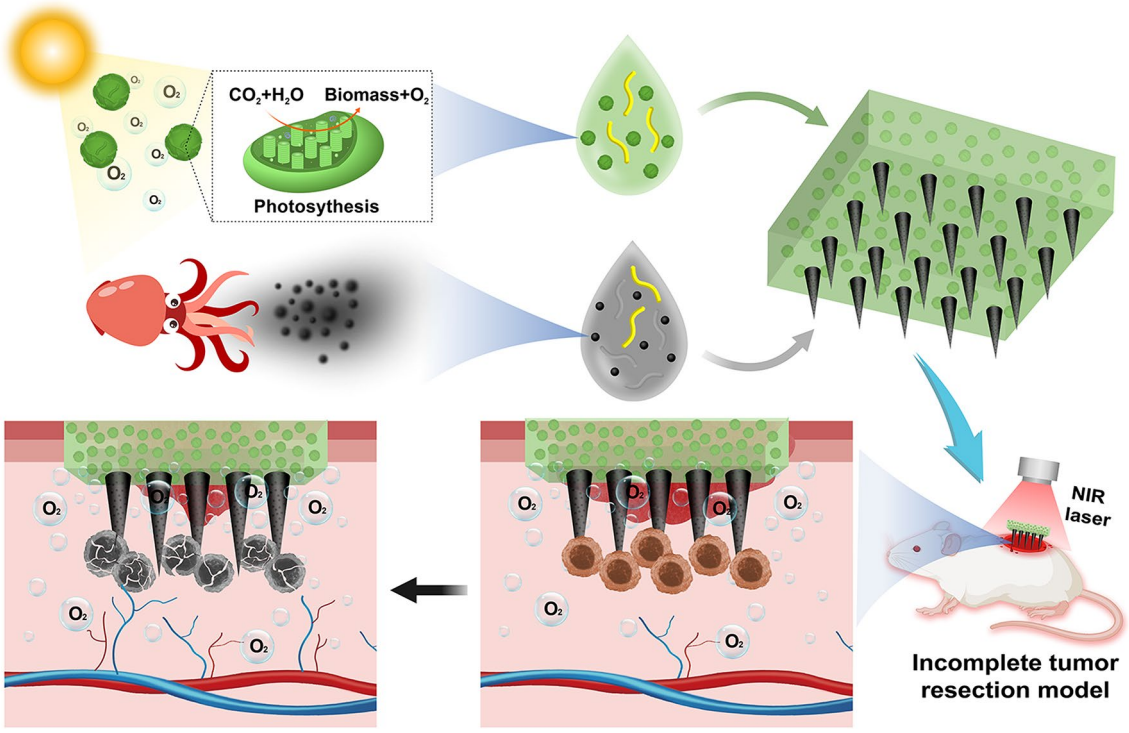

Keywords Microneedle patch, Algae, Hypoxia alleviation, Cancer therapy, Wound dressing

Introduction

Malignant melanoma is the most pernicious form of skin cancer, characterized by high invasiveness and metastatic potential [1, 2]. Predictions indicate that by the year 2040, the incidence of melanoma will increase by 50% and the mortality rate will increase by 68% [3]. Surgical excision remains the principal treatment for melanoma, while standard excision margins are often inadequate for eradicating the tumor tissue, with 80% of patients experiencing tumor recurrence or metastasis after surgery [4]. In addition, the large-scale skin defects following surgical excision are usually difficult to heal and become chronic wounds, which necessitate timely repair to relieve postoperative pain and improve the life quality of patients [5, 6]. Previous studies have indicated a promising strategy for the treatment of postoperative skin tumor wounds using bifunctional wound dressings like composite hydrogels, fibrous membranes, and bioactive glass nanoparticles [7–11]. Their treatment strategy mainly involves killing residual tumor cells through photothermal effects and promoting wound healing by utilizing their additional biological activity. However, these dressings with single photothermal effects are not sufficient to ablate residual tumor cells in deeper tissues, and thus fail to effectively prevent tumor recurrence/metastasis. Moreover, the impaired oxygen supply (i.e., hypoxia) in the tumor microenvironment may facilitate the tumor recurrence/metastasis while delaying the wound healing process [12]. Therefore, it is highly desired to develop a multifunctional wound dressing that can simultaneously kill tumor cells, alleviate hypoxia, and promote wound healing for postoperative melanoma therapy.

Herein, we proposed a multifunctional microneedle (MN) patch by incorporating alive photosynthetic algae for in situ oxygen supply and postsurgical melanoma therapy, as schemed in Fig. 1. Compared to conventional patches or needles, MN patches feature microscale needle tips on a supportive patch, offering a painless, minimally invasive, and convenient way to bypass the skin barrier for effective drug delivery in diverse applications [13–16]. Specifically, by precisely designing various template parameters, such as the arrangement of the needle array, needle density, length and diameter of the needles, tip shape, and base shape, we can prepare MNs with diverse macro- and microstructural characteristics [17–21]. Additionally, by carefully selecting the functional materials for the preparation of bases and tips, MNs can not only achieve photothermal conversion therapy but also regulate oxidative stress, provide antioxidant and antibacterial effects, and even exhibit hemostatic properties

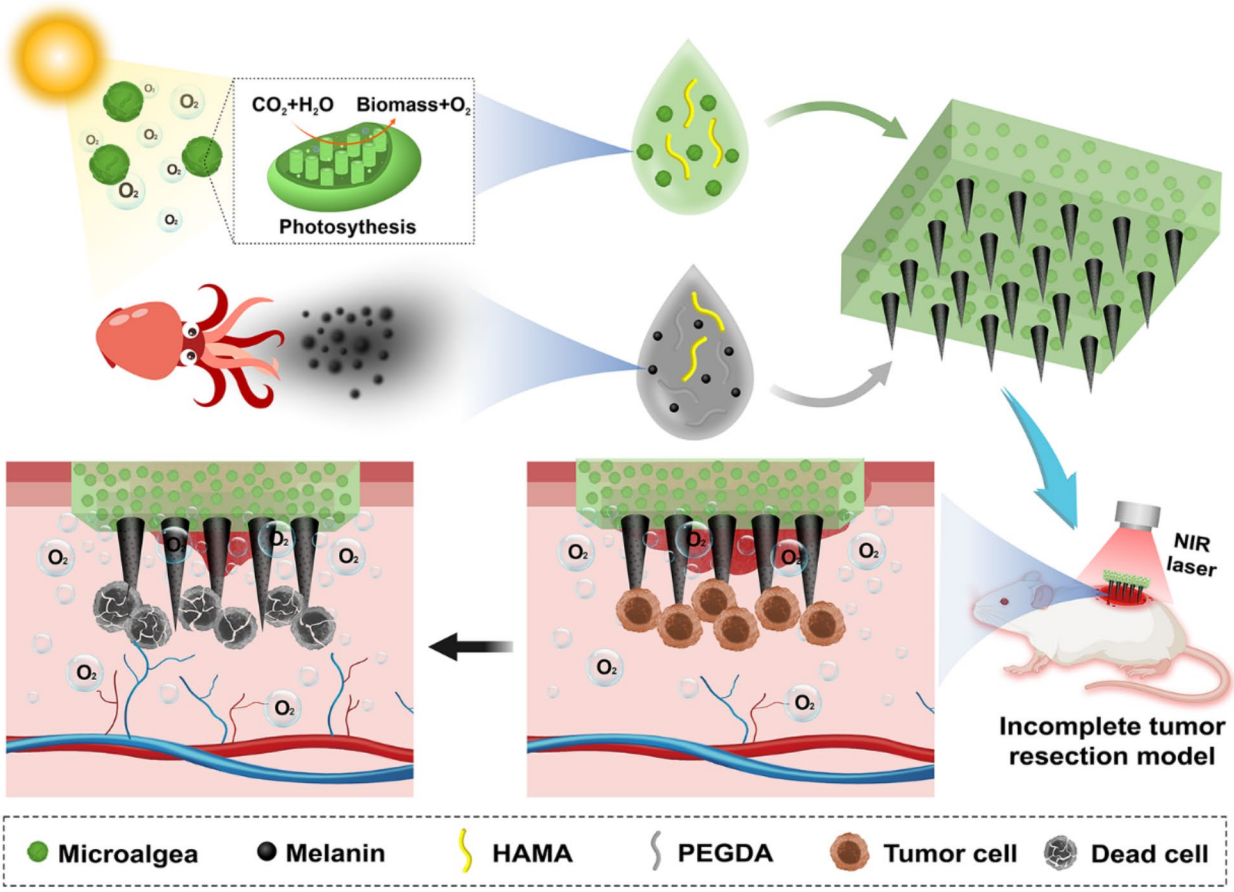

Fig. 1 Schematic illustration of the fabrication of living photosynthetic MN patches and their application for in situ oxygenation and postsurgical melanoma therapy

[22–24]. These characteristics enable MNs to meet various clinical needs, including the treatment of diabetic wounds, hemorrhagic wounds, post-surgical tumor wounds, and so on [25–27]. As a typical characteristic of tumor tissues, hypoxia can facilitate tumor progression into deep tissue layers by promoting angiogenesis, metabolic adaptation, immune evasion, metastasis, and treatment resistance [28]. Accordingly, therapeutic strategies have been proposed to alleviate hypoxia by delivering oxygen into tumor tissues or in situ generating oxygen at tumor sites [29–31]. In addition, oxygen is also an important factor for wound healing and the lack of oxygen supply can severely delay the wound healing process [32, 33]. Benefiting from their original photoenergy synthesis system, algal microbes have been employed as oxygen suppliers to alleviate hypoxia for the treatment of various hypoxic diseases such as solid tumors or chronic wounds [34–36]. Therefore, we anticipated that the incorporation of photosynthetic algae into MN systems would provide an effective strategy to inhibit tumor recurrence/spread and enhance wound recovery for postsurgical melanoma therapy.

In this study, we present the desired living photosynthetic MN patch (namely MA/CM@MN) loaded with microalgae (MA) and cuttlefish melanin (CM) for postsurgical melanoma therapy and skin wound healing (Fig. 1). As a polymer similar to skin melanin, CM has been utilized for tumor therapy due to its good biocompatibility and intrinsic photothermal properties [37–39]. The obtained MA/CM@MN was fabricated via a typical template replication method, which imparted the MN with a living MA-laden MN base for in situ oxygenation and CM-laden MN tips for photothermal therapy (PTT). Owing to the oxygenic photosynthesis of the alive MA in the MN base, the MA/CM@MN could produce oxygen under light exposure, which facilitated skin cell growth and protected the cells from hypoxia-triggered cell death. Besides, with CM nanoparticles embedded in the MN tips, the MA/CM@MN could be effectively heated up under NIR irradiation, contributing to a strong tumor killing efficacy on melanoma cells in vitro. Further in vivo experiments showed that the NIR irradiated MA/CM@MN effectively prevented local tumor recurrence and simultaneously promoted wound healing in

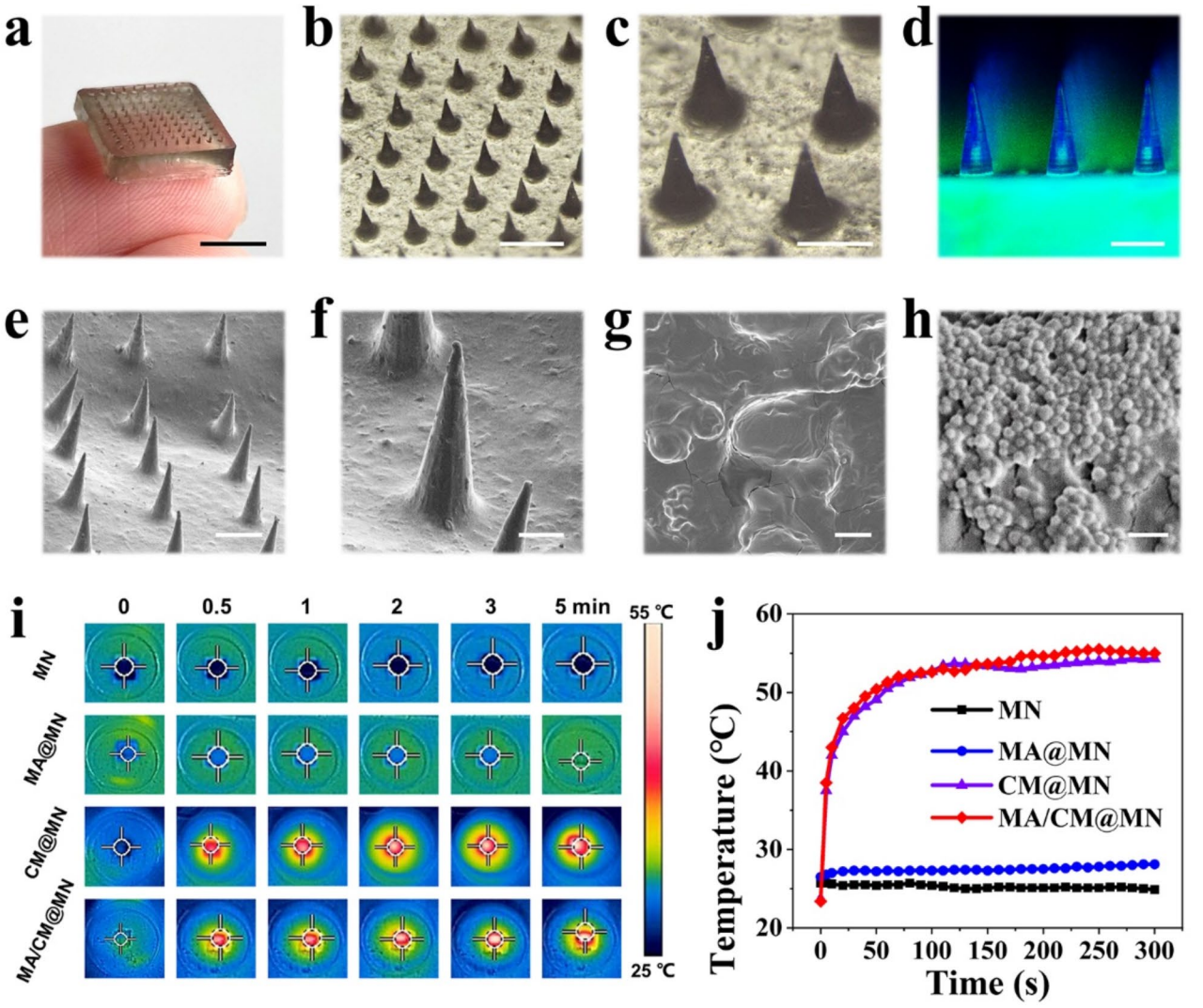

Fig. 2 Characterization of the living microalgae (MA) and cuttlefish melanin (CM)-loading MNs (MA/CM@MN). (**a**) Photographs of MA/CM@MN. Scale bars indicate 5 mm. (**b**-**c**) Optical images, (**d**) fluorescent images, and (**e**,**f**) SEM images of the MA/CM@MN at different magnifications. (**g**, **h**) High-resolution SEM images showing the MA embedded in the MN base (**g**) and CM nanoparticles dispersed in the MN tips (**h**). Scale bars indicate 1 mm in (**b**), 500 μm in (**c**, **d**), 300 μm in (**e**), 100 μm in (**f**), 5 μm in (g), and 500 nm in (h). (**i**-**j**) Real-time infrared thermal images (**i**) and corresponding photothermal heating curves (**j**) of membranes under continuous irradiation of an 808-nm laser at the power density of 0.50 W/cm^2 for 5 min

an incomplete tumor resection model, probably because the MA/CM@MN could inhibit tumor cell proliferation, stimulate tumor cell apoptosis, and mitigate tissue hypoxia in light. All these results suggested that such living photosynthetic MN patches could fulfill the multiple requirements of killing tumor cells, alleviating tumor hypoxia and promoting wound healing in postsurgical melanoma therapy.

Results and discussion

Generally, the living photosynthetic MN patches loaded with MA and CM (i.e., MA/CM@MN) were prepared via a template replication method (Figure S1). CM was extracted from food-grade squid ink, and characterized as a spherical nanoparticle with an average hydrodynamic diameter of 205.6 nm and a zeta potential of -30.1 mV. The interparticle repulsive forces facilitated the homogeneous dispersion of CM nanoparticles in an aqueous solution without precipitation for more than 24 h (Figure S2a, b). The particle size and shape of CM nanoparticles were further confirmed by SEM (Figure S2c, d). Subsequently, CM dispersed in the methacrylated hyaluronic acid (HAMA) and ethylene glycol dimethacrylate (PEGDA) solution to fabricate MN tips, while MA was dispersed in HAMA solution to prepare the MN base, resulting in the formation of MA/CM@MN (Fig. 2a and Figure S1). A 10×10 microsized needle array was neatly arranged on a 10×10 mm^2 patch, and each needle had a conical shape, featuring 350 μm in the base diameter and 900 μm in height (Fig. 2b-d). Moreover, the tips of MA/

CM@MN appeared dark gray while the base appeared light green due to the presence of CM and MA. The SEM images of lyophilized samples further confirmed the existence of MA and CM nanoparticles in the base and tips of MA/CM@MN, respectively (Fig. 2e-h and Figure S3), when compared to the smooth and flat surface of unloaded MNs (Figure S4).

Next, to explore the photothermal heating capabilities of CM-loaded MNs, we recorded the temperature fluctuations and thermographic images of MN patches in real time during continuous NIR irradiation. We found that the temperature of CM-loaded MNs (including CM@MN and MA/CM@MN) was rapidly elevated and stabilized at around 55 °C within 5 min when subjected to an 808-nm laser at 0.50 W/cm^2 (Fig. 2i, j). By contrast, the CM-unloaded MNs (including MN and MA@MN) showed no significant temperature change under the same irradiation conditions, indicating that the good photothermal performance of CM-loaded MNs was derived from the photothermal conversion capacity of CM nanoparticles as previously demonstrated [40, 41]. To verify the controllability of photothermal heating properties, a series of CM-loaded MNs with various CM concentrations were prepared and irradiated at different NIR laser power intensities. It was found that the photothermal temperature of MA/CM@MN increased with CM concentrations or laser power intensities (Figure S5a, b). Furthermore, the photothermal effect of MA/CM@MN could be well maintained after five cycles of NIR laser irradiation (Figure S5c), suggesting their high photothermal stability. Collectively, the above results demonstrated that we had successfully prepared a living photosynthetic MN patch loaded with CM and MA, which exhibited good photothermal performance and held great potential for tumor PTT.

To evaluate the photosynthetic oxygenation activity of MA/CM@MN, we cultured the MA-laden MNs (including MA@MN and MA/CM@MN) in light and continuously monitored the dissolved oxygen (DO) levels during 7 days of culture (Fig. 3a, b). Bright-field microscopy images showed a pronounced rise in the MA quantities on day 7 even for the MA/CM@MN+NIR group, which was irradiated by an NIR laser at 0.50 W/cm^2 for 5 min on days 1 and 3 (Fig. 3a). This indicated that MA well survived from the MN preparation process and maintained its proliferative capacity within the HAMA matrix, unaffected by either the CM incorporation or short-time NIR irradiation. Further analysis of the DO levels revealed that the MA-laden MNs could continuously release oxygen in light, and the amount of released oxygen increased over time as the MA proliferated well during in vitro culture (Fig. 3b).

Subsequently, the cytocompatibility of MA/CM@MN was verified by co-culturing different MNs with human skin fibroblasts (HSFs) under normoxic conditions. Live/dead staining images showed that almost all HSFs are alive when cultured with different MNs (including MN, MA@MN, CM@MN, and MA/CM@MN), even for the MA/CM@MN group exposed to short-time NIR irradiation (Fig. 3c). The result of CCK8 assay confirmed the cell proliferation of HSFs in all groups, suggesting that both the CM and MA incorporation into MN matrix had no obvious cytotoxicity to cell viability and may had a certain promotive effect on the skin cell proliferation (Fig. 3d). It was noted that although the cell viability in MA/CM@MN+NIR group was inferior to that of the other groups during the first 3 days, no significance was observed for the OD values between MA/CM@MN+NIR and control group on day 5, indicating the short-time NIR irradiation did not have long-term adverse effect on cell proliferation. While hydrogels containing MA and CM can indeed provide similar therapeutic effects, we chose to utilize the MN patch in this work for several compelling reasons. Generally, the MN patch, with its microscale needle tips, offers a painless, non-invasive, and convenient method to bypass the skin barrier, enhancing the bioavailability of therapeutic agents compared to topical hydrogels. More importantly, unlike composite hydrogels with MA and CM incorporated within a single matrix, the MN patch design enables functional partitioning between the MN base and tips. This design can effectively reduce damage to MA during the photothermal heating process associated with CM, thus preserving the viability of MA. Our results indicated that the unique structure of MN patch allowed MA to survive the MN preparation process and maintain its proliferative capacity within the HAMA matrix, unaffected by either CM incorporation or short-time NIR irradiation.

To investigate the effect of photosynthetic oxygenation of MA/CM@MN on skin cell proliferation under normoxic conditions, we cultured the HSFs with different MNs under hypoxic conditions (1% O_2). We found that the MA-laden MNs (including MA@MN and MA/CM@MN) significantly relieved the cell hypoxia for HSFs under light illumination, as compared to the abundant hypoxic cells in other groups under either light or dark conditions (Figure S6a, b). This indicated that MA-loaded MNs under light conditions could release a large amount of oxygen, and thus effectively alleviate the hypoxic status of HSFs. Live/dead staining images showed that the cells were alive after different treatments for 3 days regardless of the light illumination (Figure S6c). Further quantitative analysis for cell viability further confirmed the good biocompatibility of all MNs and the obvious promotive effect on the skin cell proliferation of MA-laden MNs (Figure S6d). We noted that the short-time NIR irradiation in the CM@MN+NIR group could significantly decrease the cell viability under hypoxic conditions, similar to that

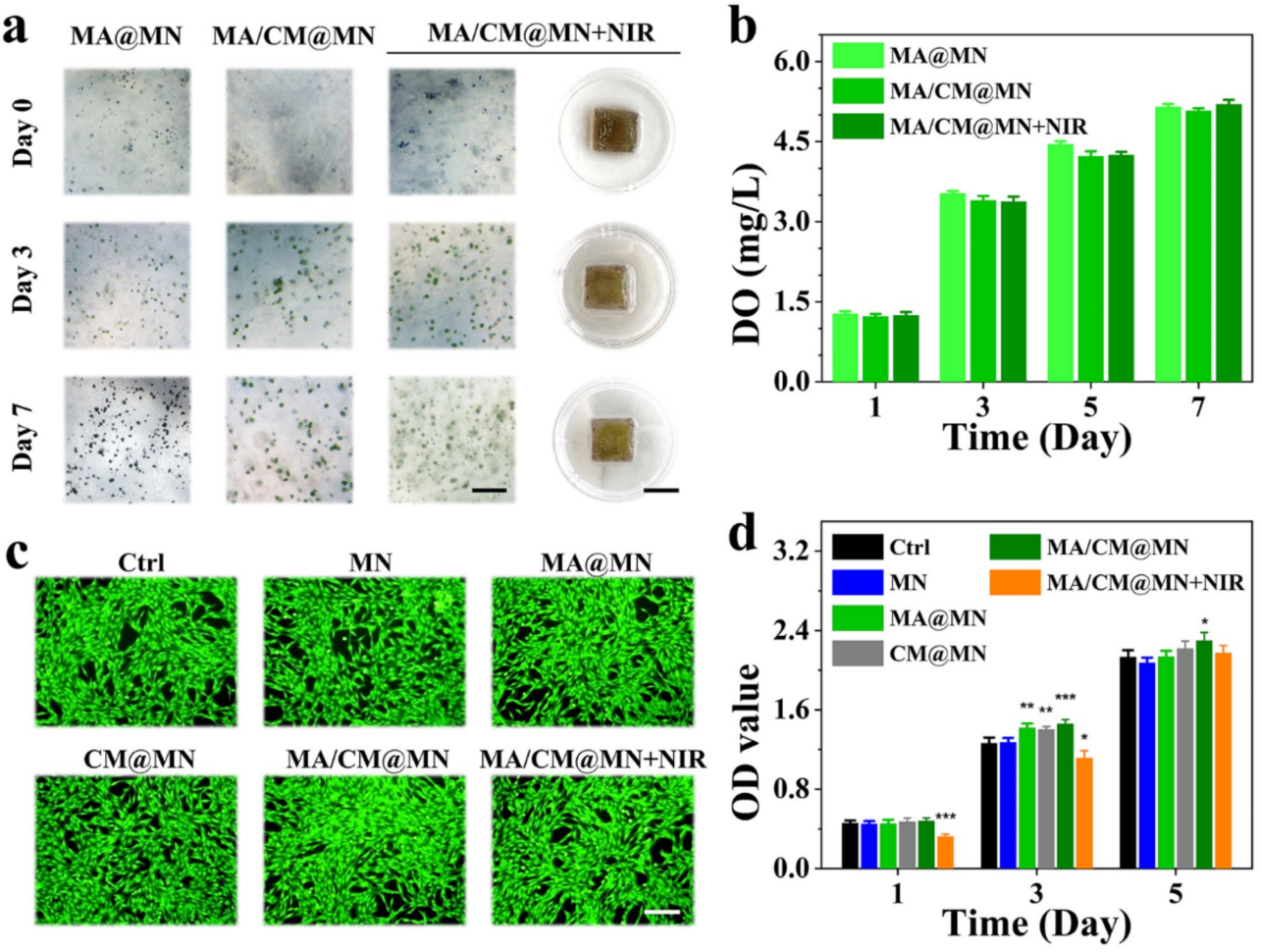

Fig. 3 Photosynthetic oxygen-generating capability of living MA-containing MNs. (**a**) Digital photographs and corresponding bright-field microscopic images of different MA-containing MNs cultivated at 25 ℃ for 7 days. Scale bars indicate 200 μm (left) and 1 cm (right). (**b**) Dissolved oxygen (DO) release in different MN groups. (**c**) Fluorescent images of human skin fibroblasts (HSFs) incubated with different MNs for 5 days under different conditions. Scale bars indicate 200 μm. (**d**) CCK8 assay of HSFs cultured in different conditions for 5 days. NIR indicates the group was treated with 808-nm irradiation at 0.50 W/cm^2 for 5 min on days 1 and 3. $N = 6$ per group, $^*p < 0.05$, $^{**}p < 0.01$, and $^{***}p < 0.001$

observed under normoxic conditions (Fig. 3d), suggesting the tumor cell killing potential of MA-laden MNs under NIR irradiation. Taken together, these results verified the good cytocompatibility and photosynthetic oxygenation of the living MA/CM@MN, which facilitated the proliferation of normal skin cells and protected the cells against hypoxia-induced cell death.

The in vitro antitumor efficacy of MNs was verified by incubating different MNs with B16F10 cells (murine melanoma cells). Live/dead cell staining showed that as compared to the Ctrl, MN, and MA@MN groups, the CM-laden MNs (including CM@MN and MA/CM@MN groups) exhibited significant cell death after NIR treatment, indicating that the embedded CM nanoparticles imparted the MNs with strong photothermal conversion capability, which effectively killed tumor cells under NIR irradiation (Fig. 4a). Quantitative data revealed that the cell viability of the CM@MN and MA/CM@MN groups with NIR irradiation was 6.58 ± 5.12% and 11.01 ± 4.24%, respectively, substantially lower than that of other groups (Fig. 4b). The results confirmed that the MA/CM@MN achieved excellent tumor PTT through CM-induced photothermal effect. Additionally, the lower cell viability in the MA/CM@MN than in the CM@MN group indicated the tumor-killing effect could be further enhanced by the photosynthetic generated O_2 from the alive MA. Moreover, the tumor cell viability was decreased when increasing the irradiation times (Fig. 4c) and irradiation duration (Fig. 4d). Collectively, these results verified the excellent and controllable PTT antitumor efficacy of MA/CM@MN in vitro.

We further explored the in vivo postsurgical tumor therapeutic potential of MA/CM@MN using an incomplete tumor resection model in B16F10-bearing mice. When the tumor volume reached ~ 100 mm^3, a circular wound with the full thickness (diameter: 10 mm)

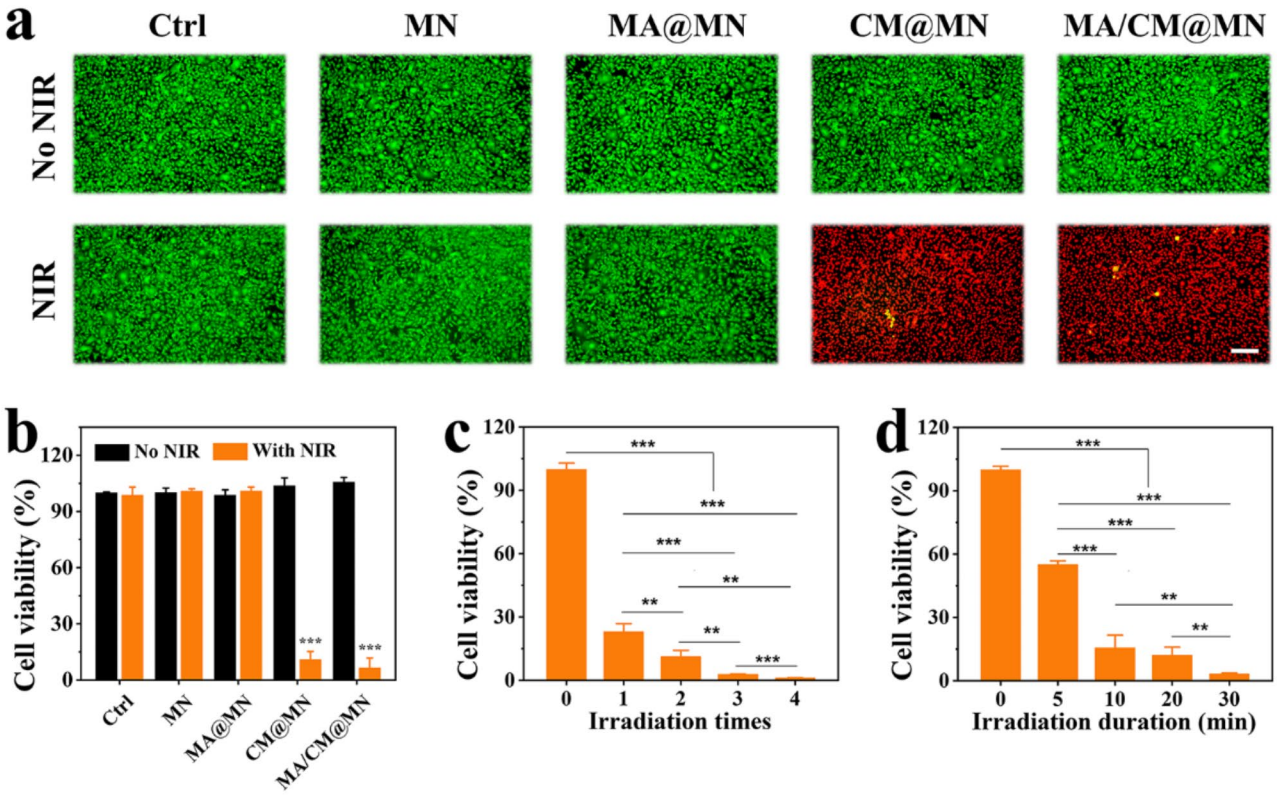

Fig. 4 In vitro photothermal antitumor therapy. (**a**) Live/dead staining of B16F10 cells after different treatments. Alive or dead cells were stained in green or red, respectively. Scale bar indicates 200 μm. (**b**-**d**) Relative cell viability of B16F10 cells treated under different conditions: (**b**) different MNs with or without NIR treatments (808 nm, 0.50 W/cm^2, 15 min); (**c**) MA/CM@MN with different irradiation duration (0.50 W/cm^2); and (**d**) MA/CM@MN with the different number of irradiation times (0.50 W/cm^2, 15 min). $N = 6$ per group, $^*p < 0.05$, $^{**}p < 0.01$, and $^{***}p < 0.001$

was created and ~90% of the tumor tissue was excised. MN, CM@MN and MA/CM@MN patches were then implanted into the tumor-induced wounds and exposed to NIR irradiation (808 nm, 0.50 W/cm^2, 15 min) for consecutive 3 days postsurgery. The temperature rapidly increased to ~55 °C in the CM@MN+NIR and MA/CM@MN+NIR groups, greatly different from the negligible temperature change in the MN+NIR group (~32 °C, Figure S7). The tumor growth and wound healing progress in various groups was monitored for 12 days. As illustrated in Fig. 5a, the tumors treated with NIR-irradiated CM-laden MNs (including CM@MN+NIR and MA/CM@MN+NIR groups) significantly diminished and their wounds even gradually healed within 12 days. In contrast, the wounds hardly healed with uncontrollable tumor expansion observed in the Control, MN+NIR, and MA/CM@MN groups (Fig. 5b). The photos of skin tumors harvested on day 12 (Fig. 5c) further confirmed the significant in vivo anticancer efficacy of CM-laden MNs via NIR-induced hyperthermia.

The tumorous wound tissues were further subjected to standard hematoxylin and eosin (HE) staining on day 12 (Fig. 5d). In remarkable contrast to the tumor-specific tissue structure and vascular malformation beneath the unrecovered epidermis noticed in Control, MN+NIR, and MA/CM@MN groups, the wounds were healed with aligned tissue architectures in the CM@MN+NIR and MA/CM@MN+NIR groups. However, distinct nodules composed of tumor cells were found adjacent to the newly-regenerated tissues in the CM@MN+NIR group, indicating the local tumor recurrence after PTT treatment. By contrast, no obvious tumor nodules were present in the MA/CM@MN+NIR group, suggesting the MA/CM@MNs could prevent tumor recurrence and achieve a long-term tumor suppression effect. These results verified our assumption that the incorporation of alive MA into the MA/CM@MN systems would provide an effective strategy to prevent tumor recurrence.

In the current study, the MA/CM@MN patches consist of two parts: (1) an MN base with MA incorporated into HAMA hydrogel, and (2) MN tips with CM nanoparticles embedded in the HAMA and PEGDA composite hydrogel. Previous studies have extensively investigated the biodegradation of hydrogels in subcutaneous implantation models in mice, demonstrating that PEGDA degrades almost completely within 4 weeks after implantation, while HAMA shows significant changes by 16 weeks [42]. The mixed HAMA and PEGDA hydrogel

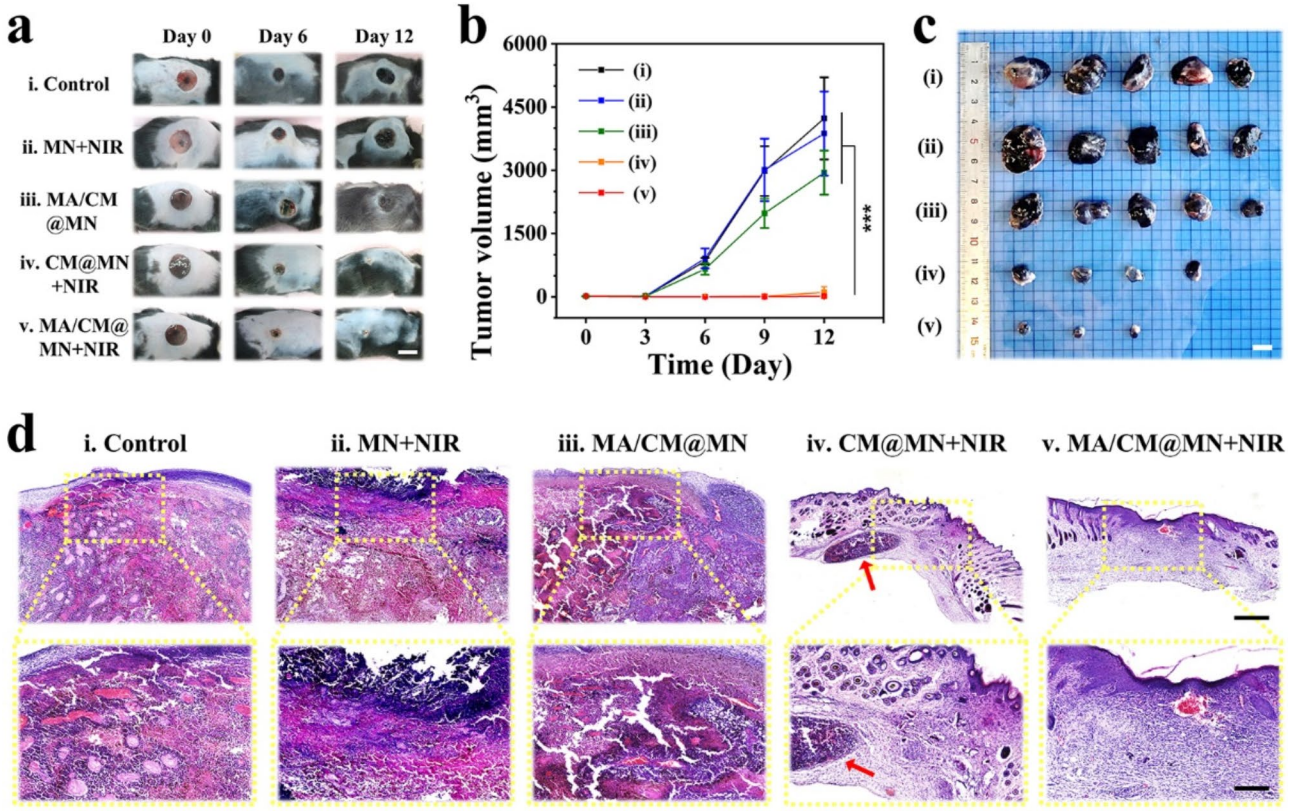

Fig. 5 In vivo antitumor therapy. (**a**) Representative photographs of the on days 0, 6, and 12 after different treatments. The scale bar indicates 1 cm. (**b**) Tumor volume changes in different groups for 12 days. $N = 6$ per group, $^{***}p < 0.001$. (**c**) Photographs of the tumors from different groups on day 12. Scale bars indicate 1 cm. (**d**) HE staining images of different groups. Scale bars indicate 500 μm (up) and 500 μm (bottom). Red arrows indicate tumor tissue nodules

can fully degrade within 4 weeks, confirming that the biodegradability of HAMA, PEGDA, and the HAMA/PEGDA composite hydrogel [43, 44]. Given that the in vivo experimental period in our study did not reach 4 weeks, we anticipate that the MNs will not fully degrade during this timeframe. In our practical in vivo experiment, the HAMA/PEGDA-composed MN tips were inserted subcutaneously for PTT, while the HAMA-composed MN base covered the wound, assisting PTT and promoting wound healing. Based on our observations, the MNs detached along with the necrotic tumor tissue and wound scab during the middle to late stages of the experimental process.

To reveal the underlying antitumor mechanism, we harvested the tumor tissues for immunofluorescence staining after 3 days of PTT treatment. The in vivo tumor cell proliferation, cell apoptosis and hypoxic tumor microenvironment were detected by Ki67 (a commonly-used cell proliferation marker), TUNEL (a method for detecting cell apoptosis), and HIF-1α (a primary marker of tissue oxygen deprivation) staining assays, respectively. Ki67 staining results indicated that the tumor cell proliferation was significantly decreased by the NIR-irradiated CM-laden MNs as compared to the control, MN+NIR and CM@MN groups, suggesting that CM-mediated PTT effectively inhibited the proliferation of remaining tumor cells (Fig. 6a, b). TUNEL staining assays revealed significantly higher cell apoptosis rates (~35%) in the CM@MN+NIR and MA/CM@MN+NIR groups than that of other groups, indicating that the NIR-induced hyperthermia played a key role in the tumor apoptosis (Fig. 6a, c).

Hypoxia is a typical hallmark of the tumor microenvironment, which facilitates cancer tumor progression and is often associated with resistance to tumor therapeutics [45]. However, oxygen plays a critical role in the normal metabolism and function of immune cells. A high-oxygen environment can enhance the activity of immune cells, enabling them to better recognize and eliminate tumor cells [46]. By contrast, under hypoxic conditions, tumor cells secrete inhibitory factors that suppress the functions of immune cells, preventing them from effectively recognizing and eliminating tumor cells [47, 48]. Additionally, hypoxia stimulates tumors to produce angiogenic factors, which not only support tumor growth but also provide a barrier for tumor cells to evade immune surveillance

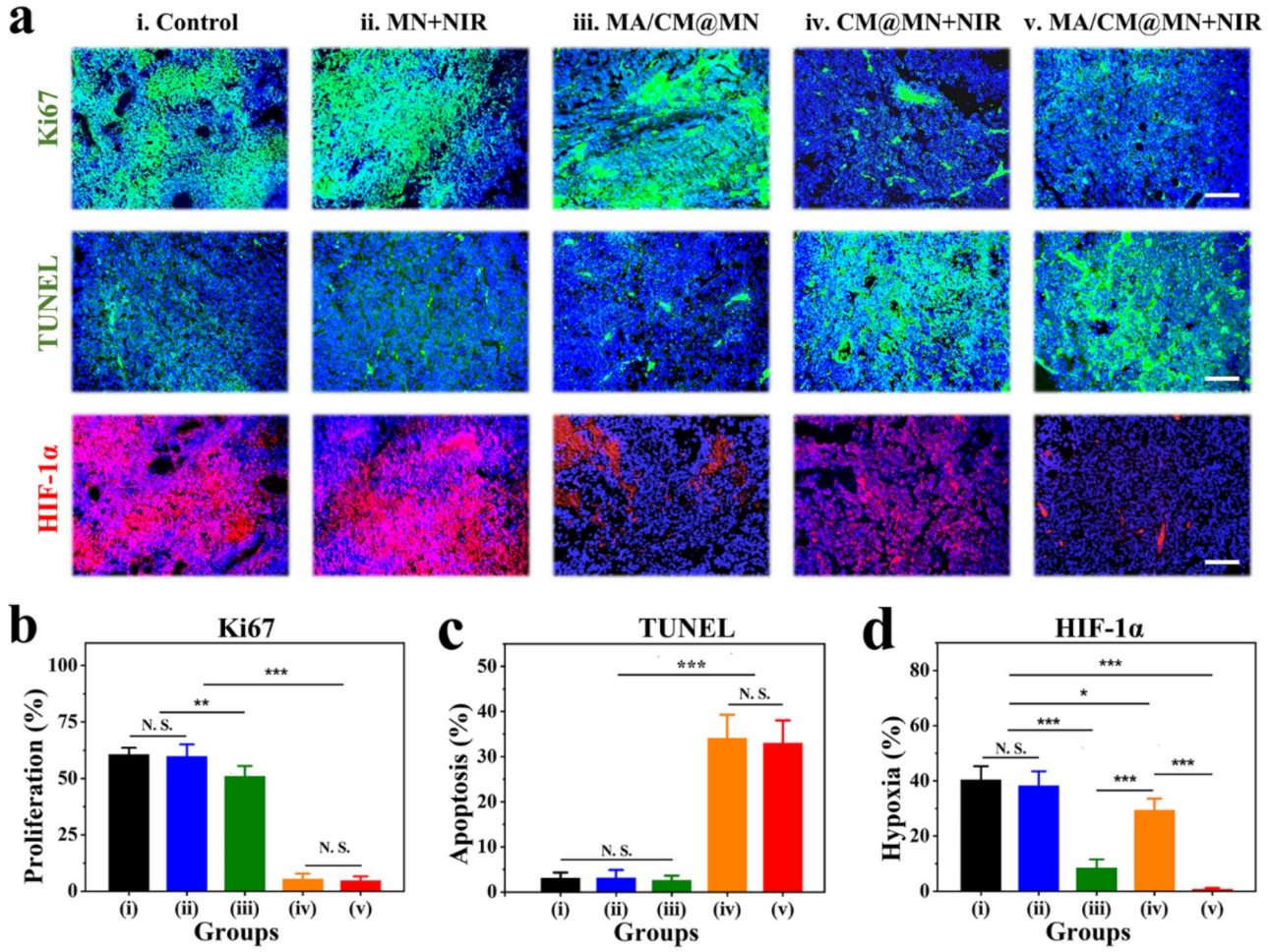

Fig. 6 In vivo microscopic antitumor efficacy. (**a**) Representative histological images of Ki67, TUNEL, and HIF-1α staining of tumor tissue sections from different groups on day 3. Scale bars indicate 200 μm. Quantification of (**b**) Ki67, (**c**) TUNEL, and (**d**) HIF-1α staining on day 3. $N = 6$ per group, N. S. indicates no significance, while $^{*}p < 0.05$, $^{**}p < 0.01$, and $^{***}p < 0.001$

[49]. Previous studies have demonstrated the feasibility of utilizing the oxygen supply materials to efficiently relieve tumor hypoxia and enhance the tumor therapeutic efficiency [50, 51]. In our study, the MA-laden MNs could continuously release oxygen through photosynthesis, effectively alleviating cell hypoxia in vitro (Figure S6). The in vivo photosynthetic oxygenation effect of the MA-laden MNs on tumor hypoxia was examined by HIF-1α staining as hypoxia can up-regulate the expression of HIF-1α [52, 53]. We found that the levels of HIF-1α expression in the MA/CM@MN (8.51±3.04%) and MA/CM@MN+NIR (0.84±0.33%) groups were notably inferior to that in the control group (40.48±4.84%), MN+NIR (38.29±5.20%), and CM@MN+NIR groups (29.49±0.33%), indicating the ameliorated tumor hypoxic microenvironment by MA-laden MNs.

Furthermore, existing studies have demonstrated that melanin can modulate the local immune microenvironment of wounds by restoring macrophage phenotypes and scavenging excess reactive oxygen species in response to near-infrared stimulation, thus improving wound healing outcomes [54, 55]. Therefore, we speculate that the CM in the needle tip of MN may not only contribute to photothermal therapy for tumors but may also have potential effects in promoting wound healing. Our in vivo results demonstrated that the MA/CM@MN could inhibit tumor cell proliferation and stimulate tumor cell apoptosis through CM-induced PTT, as well as improve the hypoxic tumor microenvironment by MA-mediated local oxygenation, which effectively prevented local tumor recurrence and simultaneously promoted wound healing for postsurgical melanoma therapy. Specifically, MN-assisted therapeutic strategies for tumor therapy have been widely studied. For example, they enhance tumor treatment by facilitating the delivery of therapeutic agents to localized cancer tissues while minimizing adverse side effects in healthy tissues [56–58]. Additionally, MNs can also carry photothermal-activated immunotherapeutic agents and deliver them to tumor sites, thereby inhibiting tumor metastasis

[59–62]. In this study, we have primarily focused on the therapeutic effects of the MA/CM@MN patches for photothermal ablation of residual tumor cells and modulation of hypoxic microenvironment in postoperative skin wounds. We recognize the importance of addressing tumor metastasis as part of a comprehensive treatment approach and have considered the incorporation of photothermal-activated immunotherapeutic agents to inhibit tumor metastasis in future studies. By combining our MN patches with such agents, we could potentially enhance the immune response against residual tumor cells, thereby reducing the risk of metastasis.

Conclusion

In the present study, we reported a living photosynthetic MN patch (i.e., MA/CM@MN) for postsurgical melanoma therapy and skin wound healing. The obtained MA/CM@MN was featured with a living MA-laden MN base and CM-laden MN tips. Due to the oxygenic photosynthesis of the alive MA, the MA/CM@MN could generate oxygen under light exposure, which promoted skin cell proliferation and protected the cells against hypoxia-induced cell death. Additionally, with CM nanoparticles embedded in the MN tips, the MA/CM@MN could be effectively heated up under NIR irradiation, resulting in a strong tumor killing efficacy on skin melanoma cells in vitro. When implanted into the wound beds after incomplete tumor resection, the MA/CM@MN could effectively prevent the local tumor recurrence and simultaneously promote wound healing. Further histological analysis revealed that the MA/CM@MN could inhibit tumor cell proliferation, trigger tumor cell apoptosis, and alleviate tissue hypoxia. These results indicate that such living photosynthetic MN patches can provide a simple and effective strategy for postoperative cancer therapy and wound healing applications.

Experimental section

Materials

Cuttlefish ink powder was purchased from Henan Zhongda Hengyuan Biotechnology. HA sodium salt (MW1.5 million Da) was purchased from Bloomage Biotechnology. Methacrylic anhydride (MA) was obtained from Sigma-Aldrich. Lithium phenyl-2,4, 6-trimethylbenzoyl phosphonate (LAP) and ethylene glycol dimethacrylate (PEGDA) were bought from Aladdin. Microalgae (MA, Chlorella pyrenoidosa) and the specialized microalgae culture medium were purchased from Nanjing Health Biotech.

Purification of cuttlefish melanin nanoparticles

Cuttlefish ink powder (14 g) was dispersed in distilled water (0.5 L) and stirred at 50 °C (1 h) to create uniform solutions, followed by centrifugation (8000 rpm, 5 min) to remove precipitates. The suspension was further filtered (0.8 μm) to remove residual large particles, followed by the centrifugation again (10000 rpm, 15 min) to remove small particles and water-soluble impurities. The obtained sediment was redispersed in distilled water, sonicated and centrifuged again (10000 rpm, 15 min). Then the sediment was redispersed in pure ethanol, sonicated, and centrifuged (10000 rpm, 15 min). The previous steps were repeated more than three times. The purified cuttlefish melanin nanoparticles (particle size around 200 nm) were finally obtained after vacuum drying at 65 °C. The particle size and zeta potential of the purified cuttlefish melanin nanoparticles were measured using a nanoparticle size analyzer (Zetasizer Nano, ZEN3600), which directly provided the particle size distribution curve and zeta potential values.

Synthesis of HAMA

Initially, a hyaluronic acid (HA) was synthesized by completely dissolving 4.0 g HA in 300 mL distilled water by stirring overnight. 5 mL of methacrylamide (MA) was dispersed in 200 mL N, N-Dimenthylformamide and then slowly dripped into the HA solution. PH was adjusted to the range of 8 to 9 during the manufacturing process. After 12 h, the solution was diluted with 1 L of deionized water and then dialyzed at 4 °C for 3 days. Finally, purified HAMA was obtained through lyophilization.

Preparation of MA/CM@MN

MN patches (MA/CM@MN) were prepared via a template replication method. The solution for MN tips was prepared by blending HAMA (5% w/v), PEGDA (4% w/v), CM (1 mg/mL), LAP (2‰ w/v) into PBS. The solution for the MN base was obtained by dispersing MA (1×10^6 cells/ mL) in the 10% (w/v) HAMA solution. 0.1 mL of needle tip solution was added into the MN mold, vacuumed (1 min), and centrifuged (3000 rpm, 5 min). The MN mold was subsequently exposed to ultraviolet light for 60 s to fabricate the MN tips. Afterwards, 200 μL of the MN base solution was added into the mold, which was subsequently exposed to ultraviolet light for 60 s. The MA/CM@MN patches were obtained after being demolded from the PDMS mold. To fabricate fluorescent MNs with distinct separation morphology between the needle tips and base, blue fluorescent nanoparticles were added to the MN tips solution, while green fluorescent nanoparticles were added to the MN base solution.

Characterization

Bright-field images and fluorescence images were captured utilizing a microscope (Olympus, SZX16). The microstructures of melanin nanoparticles and MN patches were characterized utilizing a scanning electron microscope (SEM, Hitachi SU8010).

The photothermal effect of MA/CM@MN

The photothermal performance of MA/CM@MN was tested using an 808-nm laser beam (diameter: around 12 mm, 0.50 W/cm^2) for 5 min. An infrared thermal imaging system was employed to capture real-time temperature changes. The controllable photothermal heating capacity of MA/CM@MN was evaluated by irradiating the MA@MN with varying CM contents (0, 0.25, 0.5, 1, and 2 mg/mL) using an 808-nm laser at an intensity of 0.50 W/cm^2 for 5 min. Additionally, the MA@MN with 0.5 mg/mL CM contents was irradiated under the 808-nm laser with variable power intensities (0.30, 0.40, 0.50, 0.60 and 0.70 W/cm^2) for 5 min. The photothermal stability of MA/CM@MN was assessed through repeated NIR exposure followed by natural cooling (0.50, NIR ON or OFF for 5 min, 5 cycles).

Dissolved oxygen release from the MA/CM@MN

The oxygen generation capability of the MA/CM@MN was tested under an LED light bulb. The brightness was maintained at 6000 lx with the MNs positioned 10 cm away from the light source. The MA proliferation within the MA/CM@MN was recorded every three days.

Cell biocompatibility assay

HSFs incubated overnight in 24-well plates (1×10^4 cells/well). Subsequently, Transwell inserts (0.4 μm pore-sized filters) holding an MN or MA/CM@MN were carefully placed into the plate. The MNs in each group were illuminated with the LED light for 6 h daily. Cells were exposed to the MNs for 5 days, and the proliferation status was evaluated via the CCK-8 kit. Furthermore, cells were stained using the Calcein-AM and PI staining methods.

Intracellular hypoxia alleviation

The intracellular hypoxia relief of MA/CM@MN was assessed by the red-fluorescent hypoxia marker {[Ru(dpp)$_3$]Cl$_2$}. HSFs were seeded at 24-well plates with 10^5 cells/well and incubated under normoxic conditions for 12 h. Subsequently, the cells were tranfered to hypoxic conditions (1% O_2), and transwell inserts holding an MN or MA/CM@MN were placed into the 24-well plate. The MNs in each group were illuminated with the LED light for 6 h and then kept in dark for another 6 h. After illumination, the MNs were extracted, and culture mediums were replaced with DMEM containing hypoxia indicators (8 mg/L). After incubation for 4 h, the probe solution was extracted, and the HSFs were immobilized in 4% paraformaldehyde. The cell nucleus was stained with DAPI (blue) for observation.

Cell proliferation assay

HSFs were cultured in 24-well plates (1×10^4 cells/well) overnight. Transwell inserts holding an MN or MA/CM@MN were placed into the plate. The MNs in each group were cultured under three different conditions: dark, illuminated with LED light for 6 h, and illuminated with LED light for 6 h and 808-nm laser (NIR irradiation) for 5 min. The cells were cultured under hypoxic conditions (1% O_2) with different MNs for 5 days, and cell viability was assessed using the CCK-8 assay. Moreover, live/dead assays were conducted with Calcein-AM and PI staining.

In vitro antitumor effects

The murine melanoma B16F10 cells were cultured in 24-well plates (5×10^4 cells/well) overnight. Transwell inserts holding an MN or MA/CM@MN were carefully inserted into the 24-well plate. Each group received either a 15-min NIR laser treatment or no treatment, followed by 12 h of incubation. Subsequently, the cells were subjected to live/dead staining with Calcein-AM and PI, followed by visualization under a fluorescence microscope. Cell viability was assessed by treating the cells with CCK-8 kits.

In vivo antitumor evaluation

C57BL/6 male mice (5–6 weeks old) bearing B16F10 tumors were employed to investigate the in vivo antitumor efficacy of the MA/CM@MN. The animal experimental protocol was approved by the Animal Care and Use Committee of Wenzhou Institute, University of Chinese Academy of Sciences (WIUCAS22052501). B16F10 cells (1×10^7 cells/mL) were subcutaneously injected into the right side of each mouse. Once tumor volume reached approximately 100 mm^3, a round full-thickness wound (diameter: 10 mm) was generated at tumor sites, and nearly 90% of the tumor tissue was excised, resulting in an initial tumor volume of approximately 13–15 mm^3. The puncture ability of MN tips into murine skin tissues was verified before the in vivo application of different MNs (Figure S8). Subsequently, a specific MN was pressed towards a wound area and completely covered the residual tumor tissues. The MN in the wound bed was further wrapped with a transparent membrane (3 M). NIR irradiation (808 nm, 0.50 W/cm^2) was administered 15 min once a day for 3 days post-surgery. Infrared cameras were used to record temperature changes in the wound area. Every three days, the tumor-induced wounds were photographed, and the tumor size was measured using calipers. The tumor volume (V) was caculated as $V=LW^2/2$ (L: longest diameter; W: shortest diameter). Black protuberances at wound beds were identified as tumor tissues. Part of the mice were euthanized on day 3 and the remaining mice were sacrificed on day 12. Their tumor tissues were excised and photographed. Tumor slices were treated with immunohistochemical

staining (HIF-1α, Ki67) and TUNEL assays for histological analysis.

Statistical analysis

Data are presented as means ± standard deviations ($n \geq 4$). Graphs were generated using OriginPro 2021 software. Statistical significance between the two groups was determined using two-tailed unpaired Student's t-tests, with significance denoted as $p < 0.05$ (*), $p < 0.01$ (**), and $p < 0.001$ (***).

Supplementary Information

The online version contains supplementary material available at https://doi.org/10.1186/s12951-024-02982-8.

Supplementary Material 1

Acknowledgements

This work was supported by the National Key Research and Development Program of China (2022YFA1105300), the National Natural Science Foundation of China (32201117, 52073060, 82071035, 82371165 and 61927805), the Nanjing Medical Science and Technique Development Foundation (ZKX21019), the Clinical Trials from Nanjing Drum Tower Hospital (2022-LCYJ-ZD-01), Guangdong Basic and Applied Basic Research Foundation (2021B1515120054), and Shenzhen Science and Technology Program (JCYJ20210324133214038).

Author contributions

Y.J.Z., M.Q.Z. and X.C.W. conceived the idea and designed the experiment; J.X.J. and X.C.W. conducted experiments and data analysis; X.H.G., Y.W.W. and M.L.W. participated in data collection and discussion. J.X.J. and X.C.W. wrote the manuscript.

Data availability

No datasets were generated or analysed during the current study.

Declarations

Ethics approval and consent to participate

This study has been approved by the ethics committee of the Wenzhou Institute of University of Chinese Academy of Sciences (Wenzhou, China) and conducted in accordance with ethical guidelines.

Consent for publication

All authors have provided consent for the manuscript to be published in Journal of Nanobiotechnology.

Competing interests

The authors declare no competing interests.

Author details

[1]Department of Rheumatology and Immunology, Nanjing Drum Tower Hospital, School of Pharmacy, Clinical Medical College of Traditional Chinese and Western Medicine, Nanjing University of Chinese Medicine, Nanjing 210023, China
[2]Department of Rheumatology and Immunology, The First Affiliated Hospital of Anhui Medical University, Hefei, Anhui 230022, China
[3]Department of Ultrasound Medicine, Tangdu Hospital, Air Force Medical University, Xi'an 710038, China
[4]Department of Gynaecology, The Second Affiliated Hospital and Yuying Children's Hospital, Wenzhou Medical University, Wenzhou, Zhejiang 325027, China
[5]Department of Pathology, Shandong Cancer Hospital and Institute, Shandong First Medical University and Shandong Academy of Medical Sciences, Jinan, Shangdong 250117, China
[6]Shenzhen Research Institute, Southeast University, Shenzhen 518071, China

Received: 18 August 2024 / Accepted: 4 November 2024
Published online: 11 November 2024

References

1. Luu YT, Goldstein AM, Sargen MR. Variation in second cancer risk by melanoma subtype among survivors. J Am Acad Dermatol. 2023;88:433–4.
2. Cabrita R, Lauss M, Sanna A, Donia M, Larsen MS, Mitra S, Johansson I, Phung B, Harbst K, Vallon-Christersson J, et al. Tertiary lymphoid structures improve immunotherapy and survival in melanoma. Nature. 2020;577:561–5.
3. Arnold M, Singh D, Laversanne M, Vignat J, Vaccarella S, Meheus F, Cust AE, de Vries E, Whiteman DC, Bray F. Global Burden of Cutaneous Melanoma in 2020 and projections to 2040. JAMA Dermatology. 2022;158:495–503.
4. Wen X, Li D, Zhao J, Li J, Yang T, Ding Y, Peng R, Zhu B, Huang F, Zhang X. Time-varying pattern of recurrence risk for localized melanoma in China. World J Surg Oncol. 2020;18:6.
5. Falanga V, Isseroff RR, Soulika AM, Romanelli M, Margolis D, Kapp S, Granick M, Harding K. Chronic wounds. Nat Rev Dis Primers. 2022;8:50.
6. Wang L, Sun L, Bian F, Wang Y, Zhao Y. Self-Bonded Hydrogel Inverse Opal particles as Sprayed Flexible Patch for Wound Healing. ACS Nano. 2022;16:2640–50.
7. Mi C, Dagogo Dorothy W, Min W, Wen N, Wei C, Yi G, Yidan W, Meng L, Chenxi X, Tongtong L, et al. Hierarchically multifunctional bioactive nanoglass for integrated tumor/infection therapy and impaired wound repair. Mater Today. 2022;53:27–40.
8. He D, Li H. Bifunctional Cx43 mimic peptide grafted Hyaluronic Acid Hydrogels Inhibited Tumor recurrence and stimulated Wound Healing for Postsurgical Tumor Treatment. Adv Funct Mater. 2020;30:2004709.
9. Chen X, Tao J, Zhang M, Lu Z, Yu Y, Song P, Wang T, Jiang T, Zhao X. Iota Carrageenan gold-silver NPs photothermal hydrogel for tumor postsurgical anti-recurrence and wound healing. Carbohydr Polym. 2022;298:120123.
10. Chen R, Zhao C, Chen Z, Shi X, Zhu H, Bu Q, Wang L, Wang C, He H. A bionic cellulose nanofiber-based nanocage wound dressing for NIR-triggered multiple synergistic therapy of tumors and infected wounds. Biomaterials. 2021;281:121330.
11. Zhang Q, Wang X, Kuang G, Zhao Y. Pt(IV) prodrug initiated microparticles from microfluidics for tumor chemo-, photothermal and photodynamic combination therapy. Bioact Mater. 2022;24:185–96.
12. Chen S, Luo Y, He Y, Li M, Liu Y, Zhou X, Hou J, Zhou S. In-situ-sprayed therapeutic hydrogel for oxygen-actuated Janus regulation of postsurgical tumor recurrence/metastasis and wound healing. Nat Commun. 2024;15:814.
13. Zhang X, Gan J, Fan L, Luo Z, Zhao Y. Bioinspired Adaptable Indwelling Microneedles for Treatment of Diabetic Ulcers. Adv Mater. 2023;35:e2210903.
14. Yang J, Wang X, Wu D, Yi K, Zhao Y. Yunnan Baiyao-loaded multifunctional microneedle patches for rapid hemostasis and cutaneous wound healing. J Nanobiotechnol. 2023;21:178.
15. Zhang X, Chen G, Wang Y, Zhao Y. Spatial tumor biopsy with fluorescence PCR microneedle array. Innovation. 2023;5:100538.
16. Fan L, Zhang X, Wang L, Song Y, Yi K, Wang X, Zhang H, Li L, Zhao Y. Bioinspired Porous Microneedles Dwelled Stem cells for Diabetic Wound Treatment. Adv Funct Mater. 2024;34:2316742.
17. Lu M, Zhang X, Xu D, Li N, Zhao Y. Encoded structural Color Microneedle patches for multiple screening of Wound Small molecules. Adv Mater. 2023;35:e2211330.
18. Shan J, Wu X, Che J, Gan J, Zhao Y. Reactive microneedle patches with antibacterial and dead Bacteria-trapping abilities for skin infection treatment. Adv Sci. 2024;11:e2309622.
19. Wang Y, Zhang X, Chen G, Lu M, Zhao Y. Multifunctional structural color triboelectric microneedle patches for psoriasis treatment. Matter. 2023;6:1555–68.
20. Wu X, Huang D, Xu Y, Chen G, Zhao Y. Microfluidic Templated Stem Cell Spheroid Microneedles for Diabetic Wound Treatment. Adv Mater. 2023;35:e2301064.
21. Zhang X, Cheng Y, Liu R, Zhao Y. Globefish-inspired balloon catheter with Intelligent Microneedle Coating for Endovascular Drug Delivery. Adv Sci. 2022;9:e2204497.
22. Wu D, Wu X, Luan Q, Tang Q, Fan L, Shou X, Gao X, Qian X, Zhao Y. Dynamic hydrogel-integrated microneedle patch with extracellular vesicles encapsulation for wound healing. Chem Eng J. 2024;493:152252.

23. Kong B, Liu R, Shan J, Li M, Zhou X, Zhao Y. Frozen reinforced microneedles loaded with NIR-photothermal nanozyme for keratitis treatment. Nano Today. 2023;52:102000.
24. Zeng J, Lu M, Wang Y, Zhao X, Zhao Y. Photothermal fish gelatin-graphene Microneedle patches for Chronic Wound Treatment. Small. 2024; 2405847.
25. Song C, Wu X, Wang J, Liu R, Zhao Y. Photosensitizer-immunotherapy integrated microneedles for preventing tumor recurrence and metastasis. Nano Today. 2023;51:101913.
26. Yi K, Yu Y, Fan L, Wang L, Wang Y, Zhao Y. Gold nanoclusters encapsulated microneedle patches with antibacterial and self-monitoring capacities for wound management. Aggregate. 2024;5:e509.
27. Zhang Y, Zhang X, Wu X, Zhao Y. Photo-responsive polydopamine nanozyme microneedles with oxidative stress regulation ability for atopic dermatitis treatment. Nano Today. 2024;56:102241.
28. Liao C, Liu X, Zhang C, Zhang Q. Tumor hypoxia: from basic knowledge to therapeutic implications. Semin Cancer Biol. 2023;88:172–86.
29. Zou M-Z, Liu W-L, Chen H-S, Bai X-F, Gao F, Ye J-J, Cheng H, Zhang X-Z. Advances in nanomaterials for treatment of hypoxic tumor. Natl Sci Rev. 2020;8:nwaa160.
30. Zhang S, Li Z, Wang Q, Liu Q, Yuan W, Feng W, Li F. An NIR-II Photothermally Triggered Oxygen Bomb for hypoxic Tumor programmed Cascade Therapy. Adv Mater. 2022;34:e2201978.
31. Cheng Y, Kong X, Chang Y, Feng Y, Zheng R, Wu X, Xu K, Gao X, Zhang H. Spatiotemporally synchronous oxygen self-supply and reactive oxygen Species Production on Z-Scheme heterostructures for hypoxic tumor therapy. Adv Mater. 2020;32:e1908109.
32. Lee P, Chandel NS, Simon MC. Cellular adaptation to hypoxia through hypoxia inducible factors and beyond. Nat Rev Mol Cell Biol. 2020;21:268–83.
33. Yang J, Jin X, Liu W, Wang W. A programmable oxygenation device facilitates Oxygen Generation and Replenishment to promote Wound Healing. Adv Mater. 2023;35:2305819.
34. Zhong D, Du Z, Zhou M, Algae. A natural active material for biomedical applications. VIEW. 2021;2:20200189.
35. Chen H, Cheng Y, Tian J, Yang P, Zhang X, Chen Y, Hu Y, Wu J. Dissolved oxygen from microalgae-gel patch promotes chronic wound healing in diabetes. Sci Adv. 2020;6:eaba4311.
36. Qiao Y, Yang F, Xie T, Du Z, Zhong D, Qi Y, Li Y, Li W, Lu Z, Rao J, et al. Engineered algae: a novel oxygen-generating system for effective treatment of hypoxic cancer. Sci Adv. 2020;6:eaba5996.
37. Lei Q, He D, Ding L, Kong F, He P, Huang J, Guo J, Brinker CJ, Luo G, Zhu W, Yu Y. Microneedle Patches Integrated with Biomineralized melanin nanoparticles for simultaneous skin Tumor Photothermal Therapy and Wound Healing. Adv Funct Mater. 2022;32:2113269.
38. Zhang J, Shi C, Shan F, Shi N, Ye W, Zhuo Y, Zhang Y, Zhang Z, Shi Y, Peng C. From Biology to Biology: hematoporphyrin-melanin nanoconjugates with synergistic Sonodynamic-Photothermal effects on malignant tumors. Chem Eng J. 2020;408:127282.
39. Yi X, Dongdong W, Ban L, Xue C, Yuzhu Y, Cheng S, Meichan W, Puze L, Xuyu L, Hong Z, et al. In-situ synthesis of melanin in tumor with engineered probiotics for hyperbaric oxygen-synergized photothermal immunotherapy. Nano Today. 2022;47:101632.
40. Jiang Q, Liu Y, Guo R, Yao X, Sung S, Pang Z, Yang W. Erythrocyte-cancer hybrid membrane-camouflaged melanin nanoparticles for enhancing photothermal therapy efficacy in tumors. Biomaterials. 2019;192:292–308.
41. Deng R-H, Zou M-Z, Zheng D, Peng S-Y, Liu W, Bai X-F, Chen H-S, Sun Y, Zhou P-H, Zhang X-Z. Nanoparticles from Cuttlefish Ink inhibit Tumor Growth by synergizing Immunotherapy and Photothermal Therapy. ACS Nano. 2019;13:8618–29.
42. Freedman BR, Uzun O, Luna NMM, Rock A, Clifford C, Stoler E, Ostlund-Sholars G, Johnson C, Mooney DJ. Degradable and removable tough adhesive hydrogels. Adv Mater. 2021;33:e2008553.
43. Chen J, Jing Y, Liu Y, Luo Y, He Y, Qiu X, Zhang Q, Xu H. Molecularly imprinted Macroporous Hydrogel promotes bone regeneration via osteogenic induction and osteoclastic inhibition. Adv Healthc Mater. 2024;13:2400897.
44. Ma W, Zhang X, Liu Y, Fan L, Gan J, Liu W, Zhao Y, Sun L. Polydopamine decorated microneedles with Fe-MSC-Derived Nanovesicles Encapsulation for Wound Healing. Adv Sci. 2022;9:2103317.
45. Jing X, Yang F, Shao C, Wei K, Xie M, Shen H, Shu Y. Role of hypoxia in cancer therapy by regulating the tumor microenvironment. Mol Cancer. 2019;18:157.
46. Yang Z, Luo Y, Yu H, Liang K, Wang M, Wang Q, Yin B, Chen H. Reshaping the Tumor Immune Microenvironment based on a light-activated nanoplatform for efficient Cancer therapy. Adv Mater. 2021;34:e2108908.
47. Xu B, Cui Y, Wang W, Li S, Lyu C, Wang S, Bao W, Wang H, Qin M, Liu Z, et al. Immunomodulation-enhanced nanozyme-based Tumor Catalytic Therapy. Adv Mater. 2020;32:e2003563.
48. Ren Y, Wang R, Weng S, Xu H, Zhang Y, Chen S, Liu S, Ba Y, Zhou Z, Luo P, et al. Multifaceted role of redox pattern in the tumor immune microenvironment regarding autophagy and apoptosis. Mol Cancer. 2023;22:130.
49. He H, Xiao L, Wang J, Guo D, Lu Z. Aerobic glycolysis promotes tumor immune evasion and tumor cell stemness through the noncanonical function of hexokinase 2. Cancer Commun. 2023;43:387–90.
50. Yang S, Tang Z, Hu C, Zhang D, Shen N, Yu H, Chen X. Selectively potentiating hypoxia levels by Combretastatin A4 nanomedicine: toward highly enhanced hypoxia-activated Prodrug Tirapazamine Therapy for metastatic tumors. Adv Mater. 2019;31:e1805955.
51. Hao L, Wang L, Ma Y, Bottini M, Li L, Cheng H-B, Gao S, Liang X-j, Zhang J. Nanomaterials relieving hypoxia for enhanced tumor therapy. Coord Chem Rev. 2023;499:215482.
52. Ni J, Wang X, Stojanovic A, Zhang Q, Wincher M, Bühler L, Arnold A, Correia MP, Winkler M, Koch P-S, et al. Single-cell RNA sequencing of Tumor-infiltrating NK cells reveals that inhibition of transcription factor HIF-1α unleashes NK Cell activity. Immunity. 2020;52:1075–e10871078.
53. Ding X, Yu J, Hu M. The relationship between expression of PD-L1 and HIF-1α in glioma cells under hypoxia. J Clin Oncol. 2021;39:e14043–14043.
54. Bi S, He C, Zhou Y, Liu R, Chen C, Zhao X, Zhang L, Cen Y, Gu J, Yan B. Versatile conductive hydrogel orchestrating neuro–immune microenvironment for rapid diabetic wound healing through peripheral nerve regeneration. Biomaterials. 2024;314:122841.
55. Qi X, Cai E, Xiang Y, Zhang C, Ge X, Wang J, Lan Y, Xu H, Hu R, Shen J. An Immunomodulatory Hydrogel by Hyperthermia-assisted Self-Cascade glucose depletion and ROS scavenging for Diabetic Foot Ulcer Wound therapeutics. Adv Mater. 2023;35:e2306632.
56. Katherine W, Ahmed Ezat El Z, Volkan IS, Thales P. The pleiotropic functions of reactive oxygen species in cancer. Nat Cancer. 2024;5:384–99.
57. Ankang H, Li S, Hao L, Yuheng L, Hui Y, Ying M. Harnessing innate immune pathways for therapeutic advancement in cancer. Signal Transduct Target Ther. 2024;9:68.
58. Kuang G, Zhang Q, Yu Y, Shang L, Zhao Y. Cryo-shocked cancer cell microgels for tumor postoperative combination immunotherapy and tissue regeneration. Bioact Mater. 2023;18:9176–86.
59. Li D, Hu D, Xu H, Patra HK, Liu X, Zhou Z, Tang J, Slater N, Shen Y. Progress and perspective of microneedle system for anti-cancer drug delivery. Biomaterials. 2021;264:120410.
60. Chen M, Yang D, Sun Y, Liu T, Wang W, Fu J, Wang Q, Bai X, Quan G, Pan X, Wu C. Situ Self-Assembly Nanomicelle microneedles for enhanced photoimmunotherapy via Autophagy Regulation Strategy. ACS Nano. 2021;15:3387–401.
61. Yang D, Chen M, Sun Y, Jin Y, Lu C, Pan X, Quan G, Wu C. Microneedle-mediated transdermal drug delivery for treating diverse skin diseases. Acta Biomater. 2021;121:119–33.
62. Hao Y, Chen Y, He X, Yang F, Han R, Yang C, Li W, Qian Z. Near-infrared responsive 5-fluorouracil and indocyanine green loaded MPEG-PCL nanoparticle integrated with dissolvable microneedle for skin cancer therapy. Bioact Mater. 2020;5:542–52.

Publisher's note